Commun. Comput. Phys.
doi: 10.4208/cicp.010111.230911a

Vol. **12**, No. 4, pp. 1006-1032
October 2012

A Strong Stability-Preserving Predictor-Corrector Method for the Simulation of Elastic Wave Propagation in Anisotropic Media

D. H. Yang[1,*], N. Wang[1] and E. Liu[2]

[1] *Department of Mathematical Sciences, Tsinghua University, Beijing 100084, P. R. China.*
[2] *Department of Geophysics, China University of Mining and Technology, Xuzhou, Jiangsu Province, P. R. China.*

Received 1 January 2011; Accepted (in revised version) 23 September 2011

Communicated by Lianjie Huang

Available online 28 March 2012

Abstract. In this paper, we propose a strong stability-preserving predictor-corrector (SSPC) method based on an implicit Runge-Kutta method to solve the acoustic- and elastic-wave equations. We first transform the wave equations into a system of ordinary differential equations (ODEs) and apply the local extrapolation method to discretize the spatial high-order derivatives, resulting in a system of semi-discrete ODEs. Then we use the SSPC method based on an implicit Runge-Kutta method to solve the semi-discrete ODEs and introduce a weighting parameter into the SSPC method. On top of such a structure, we develop a robust numerical algorithm to effectively suppress the numerical dispersion, which is usually caused by the discretization of wave equations when coarse grids are used or geological models have large velocity contrasts between adjacent layers. Meanwhile, we investigate the performance of the SSPC method including numerical errors and convergence rate, numerical dispersion, and stability criteria with different choices of the weighting parameter to solve 1-D and 2-D acoustic- and elastic-wave equations. When the SSPC is applied to seismic simulations, the computational efficiency is also investigated by comparing the SSPC, the fourth-order Lax-Wendroff correction (LWC) method, and the staggered-grid (SG) finite difference method. Comparisons of synthetic waveforms computed by the SSPC and analytic solutions for acoustic and elastic models are given to illustrate the accuracy and the validity of the SSPC method. Furthermore, several numerical experiments are conducted for the geological models including a 2-D homogeneous transversely isotropic (TI) medium, a two-layer elastic model, and the 2-D SEG/EAGE salt model. The results show that the SSPC can be used as a practical tool for large-scale seismic simulation because of its effectiveness in suppressing numerical dispersion even in the situations such as coarse grids, strong interfaces, or high frequencies.

*Corresponding author. *Email addresses:* dhyang@math.tsinghua.edu.cn (D. H. Yang), happyxiaoxi114@163.com (N. Wang), eliu0103@hotmail.com (E. Liu)

AMS subject classifications: 65M06, 65M12, 86-08, 86A15

Key words: SSPC method, seismic wavefield modeling, anisotropy, numerical dispersion, shear-wave splitting.

1 Introduction

The development of good numerical methods is always important for both forward modeling and inverse problems (e.g. reverse time migration in exploration geophysics). Many numerical methods have been developed and widely applied in seismology. The Finite difference (FD) method such as compact FD methods (e.g. [5, 9, 16, 24]) and staggered-grid FD methods [8, 26] are widely used because of their fast speed and low computational memory for the same grid-point number, but they suffer from serious numerical dispersion when too coarse grids are chosen or too few samples per wavelength are used. The finite-element method (FEM) [4, 21, 25, 27] is a variational method which can flexibly handle variable boundary conditions with complex topography, but it requires solving large-scale linear algebraic equations at each step of time advancing which leads to large amounts of direct-access memory and computational time. The spectral method has a good property of exponential convergence rate by introducing a global basis. However, it requires the fast Fourier transform (FFT) which is time consuming, and it is also affected by numerical dispersion in time [13, 14, 29]. The spectral element method (SEM) [13,14,17,18] solves the wave equations in a framework of variational method and introduces a high accuracy of spectral techniques. The SEM inherits the advantages of both the FEM and spectral method for its exponential convergence rate and high accuracy. Although the SEM uses some diagonalizing skills to reduce the bandwidth of its mass matrix, it still needs to solve a system of linear algebraic equations at each time step, resulting in costly calculation time.

Many researchers have concerned with reducing the numerical dispersion in wavefield modeling especially when coarse grids are used or models have large velocity contrasts [2,7,20,28,33,34]. Roughly speaking, numerical dispersion is actually an unphysical waves caused by the discretization of the wave equations in which the numerical wave-velocity depends on spatial and time increments, and frequency. This unphysical wave oscillation affects our recognition of seismic-wave propagation. In some extend, high-order finite difference methods can reduce the numerical dispersion, but they usually involve more grid points in a spatial direction, resulting in both the difficulty of artificial boundary treatments and reducing the efficiency for parallel calculations. The flux-corrected transport (FCT) technique was proposed to eliminate the numerical dispersion, but it cannot fully recover the lost resolution when too coarse grids are used [7,28]. To effectively suppress the numerical dispersion to solve acoustic- and elastic-wave equations, the so-called "nearly analytic discrete method (NADM)" and its improved versions have been developed in recent years by Yang *et al.* (e.g. [3, 29–31]). Owing to the validity of

these methods in decreasing the numerical dispersion even for coarse grids, these methods can greatly reduce computational time and save memory when the coarser grids are used.

Improving the stability or the maximum Courant number of numerical methods is also attractive as it can effectively save CPU time in seismic modeling especially for high dimensional cases. The implicit methods are the natural choice for their promising theoretical stability. However, when implicit methods are used, we usually need to solve a system of large-scale linear algebraic equations at each time step, resulting in requiring memory space and computational time. In order to avoid solving the large-scale linear algebraic equations, the explicit techniques such as the predictor-corrector skills are developed to change the implicit method into an explicit scheme, which may not only avoid solving linear equations, but also inherit a good stability property of the implicit scheme.

In this paper we propose a strong stability-preserving predictor-corrector method (SSPC) to suppress the numerical dispersion caused by discretizing wave equations. The method follows the three steps: (1) the wave equation is transformed into a system of ordinary differential equations (ODEs); (2) a local interpolation method is used to discretize the spatial differential operators on the right hand of the ODEs so that we obtain a semi-discrete ODEs with respect to time, and (3) an implicit Runge-Kutta method associated with a strong stability-preserving predictor-corrector method is used to solve the semi-discrete ODEs. A systematic study of the theoretical and numerical aspects of the SSPC is carried out to include the study of errors, stability criteria for different weights, numerical dispersion, and computational efficiency. We also extend the SSPC method to anisotropic media. Numerical results using the SEG/EAGE salt model show that the SSPC can effectively suppress the numerical dispersion even for these cases of coarse grids, high frequency, and large velocity contrasts between adjacent layers. In addition, we show that the SSPC can significantly reduce the computational time and save memory.

2 Strong stability-preserving predictor-corrector method

2.1 Transform of wave equation

In 2-D heterogeneous media, the seismic wave equations can be written as

$$\rho\frac{\partial^2 U}{\partial t^2}=\nabla\cdot\sigma+f, \tag{2.1a}$$

$$\sigma=C:\varepsilon, \tag{2.1b}$$

$$\varepsilon=\frac{1}{2}[\nabla U+(\nabla U)^T], \tag{2.1c}$$

where ρ denotes the density, $U=(u_1,u_2,u_3)^T$ is the displacement vector, σ and ε are the second-order symmetric stress and strain tensors, respectively, C is the fourth-order stiff-

ness tensor, and $f=(f_1,f_2,f_3)^T$ is the external source force. We can rewrite Eq. (2.1) as follows

$$\rho\frac{\partial^2 U}{\partial t^2}=D\cdot U+f, \tag{2.2}$$

where D is a second-order partial differential operator. For example, for the 2-D homogeneous acoustic equation, the operator D is defined by

$$D=c^2\left(\frac{\partial^2}{\partial x^2}+\frac{\partial^2}{\partial z^2}\right),$$

in which c denotes the acoustic wave velocity. Let

$$W=\frac{\partial U}{\partial t}=\left(\frac{\partial u_1}{\partial t},\frac{\partial u_2}{\partial t},\frac{\partial u_3}{\partial t}\right)^T,$$

then Eq. (2.2) can be written as

$$\frac{\partial U}{\partial t}=W, \tag{2.3a}$$

$$\frac{\partial W}{\partial t}=\frac{1}{\rho}D\cdot U+\frac{1}{\rho}f. \tag{2.3b}$$

Let $V=(U,W)^T$, Eq. (2.3) is rewritten as

$$\frac{\partial V}{\partial t}=L\cdot V+F, \tag{2.4}$$

where

$$L=\begin{bmatrix}0 & I\\ \frac{1}{\rho}D & 0\end{bmatrix},\qquad F=\begin{pmatrix}0\\ \frac{1}{\rho}f\end{pmatrix}.$$

In homogeneous media, we can obtain the following equations from Eq. (2.4),

$$\frac{\partial^2 V}{\partial t\partial x}=L\cdot V_x, \tag{2.5a}$$

$$\frac{\partial^2 V}{\partial t\partial z}=L\cdot V_z, \tag{2.5b}$$

where $V_x=\partial V/\partial x$ and $V_z=\partial V/\partial z$. Let

$$\overline{V}=(V,V_x,V_z)^T,\qquad \overline{F}=(F,0,0)^T,\qquad \overline{L}=diag(L,L,L),$$

then from Eqs. (2.4) and (2.5) we have the following equation

$$\frac{\partial\overline{V}}{\partial t}=\overline{L}\cdot\overline{V}+\overline{F}. \tag{2.6}$$

2.2 Formulation of the SSPC method

The first step towards solving Eq. (2.6) is to discretize the spatial operator $\overline{L}$ included in the right-hand side of Eq. (2.6) so that a system of semi-discrete ordinary differential equations (ODEs) with respect to time is obtained. Here, we apply the local interpolation method [15, 30] to discretize the high-order spatial operator $\overline{L}$, and the computational formulae for these second- and third-order derivatives used in our present study are listed in Appendix A. After the discretization of the spatial operator $\overline{L}$, Eq. (2.6) becomes a system of semi-discrete ODEs. We then use the following diagonal implicit Runge-Kutta method [12] to solve the semi-discrete ODEs,

$$\overline{V}^{n+1}=\overline{V}^n+\frac{\Delta t}{2}(K^n+\overline{K}^n), \tag{2.7a}$$

$$K^n=\overline{L}(\overline{V}^n+r\Delta tK^n)+F(t_n+r\Delta t), \tag{2.7b}$$

$$\overline{K}^n=\overline{L}(\overline{V}^n+(1-2r)\Delta tK^n+r\Delta t\overline{K}^n)+F(t_n+(1-r)\Delta t), \tag{2.7c}$$

where $r=1/2-\sqrt{3}/6$.

To obtain the value of $\overline{V}^{n+1}$ in Eq. (2.7a), we need to compute K^n and $\overline{K}^n$ included in Eqs. (2.7b) and (2.7c) which are the slopes of the unknown function $\overline{V}$ at time $t_n+r\Delta t$ and $t_n+(1-r)\Delta t$, respectively. In another we have to sole two systems of linear algebraic equations of (2.7b) and (2.7c) to determine the two slopes of K^n and $\overline{K}^n$, which will greatly increase the computational costs. To avoid solving two systems of linear equations, we try to change the implicit Runge-Kutta schemes (2.7b) and (2.7c) into an explicit algorithm using the idea of the strong stability-preserving m-step Runge-Kutta method [22, 23] which is actually a m-step predictor-corrector method. The details are described below. We can transform Eq. (2.7b) into the m-step explicit Runge-Kutta algorithm or the so-called m-step predictor-corrector method as follows

$$K^{(0)}=\overline{L}\,\overline{V}^{(n)}, \tag{2.8a}$$

$$K^{(i)}=\sum_{k=0}^{i-1}\Big(\alpha_{i,j}K^{(k)}+r\Delta t\beta_{i,j}L(K^{(k)})\Big),\quad \alpha_{i,j}\geq 0,\quad i=1,2,\cdots,m, \tag{2.8b}$$

$$K^n=K^{(m)}+F(t_n+r\Delta t), \tag{2.8c}$$

where these parameters $\alpha_{i,j}\geq 0$ satisfy the following consistency condition

$$\sum_{k=0}^{i-1}\alpha_{i,j}=1. \tag{2.9}$$

Meanwhile, Gottlieb *et al.* [10] conclude that the m-step Runge-Kutta method is a strong stability-preserving (SSP) scheme when the coefficients of the scheme satisfy the following nonnegative conditions

$$\beta_{i,j}\geq 0 \quad \text{for all } i,j.$$

In the present study, we choose $m=2$ and other parameters in Eq. (2.8) are chosen as $\alpha_{1,0}=1$, $\beta_{1,0}=1$, $\alpha_{2,0}=\eta$, $\alpha_{2,1}=1-\eta$, $\beta_{2,0}=0$, $\beta_{2,1}=1$ where $\eta\in[0,1]$. Under the case of our consideration, the two-step predictor-corrector Runge-Kutta method (2.8) is a strong stability-preserving (SSP) scheme to solve seismic wave equation (2.6). We will confirm this statement in the later sections.

Obviously, the SSP predictor-corrector (SSPC) method (2.8) includes one prediction step (2.8a) and two correction steps (2.8b). Using Eqs. (2.8a)-(2.8c), we can explicitly compute the slope $K_{i,j}^n$ in Eq. (2.7b).

Next, we transform Eq. (2.7c) into an explicit algorithm to compute another slope $\overline{K}^n$. We first define $\overline{W}^n=\overline{V}^n+(1-2r)\Delta t K^n$, then Eq. (2.7c) can be rewritten as

$$\overline{K}^n=\overline{L}(\overline{W}^n+r\Delta t\overline{K}^n)+F(t_n+(1-r)\Delta t). \tag{2.10}$$

Similar to Eq. (2.7b), we can treat with the implicit equation (2.10) or (2.7c) to obtain the two-step predictor-corrector scheme with a parameter η as follows

$$\overline{K}^{(0)}=\overline{L}\,\overline{W}^{(n)}, \tag{2.11a}$$

$$\overline{K}^{(i)}=\sum_{m=0}^{i-1}\left(\alpha_{i,j}\overline{K}^{(m)}+r\Delta t\beta_{i,j}L(\overline{K}^{(m)})\right),\quad \alpha_{i,j}\geq 0,\quad i=1,2, \tag{2.11b}$$

$$\overline{K}^n=\overline{K}^{(2)}+F(t_n+(1-r)\Delta t), \tag{2.11c}$$

where the coefficients in Eq. (2.11) are the same as those in Eq. (2.8). Combining Eq. (2.7a) with Eqs. (2.8) and (2.11), we obtain the explicit SSPC method and can compute the value of $\overline{V}^{n+1}$ at the $(n+1)$ time step.

After the analysis of the structure of the SSPC method, we find that the SSPC degenerates to the IRK-DSM [31] when the parameter $\eta=1$ in Eqs. (2.8) and (2.11). It means that the IRK-DSM is a special case of the SSPC method. In other words, the SSPC is an extension of the IRK-DSM. When the parameter η in Eqs. (2.8) and (2.11) varies between 0 and 1, the SSPC may have different stability properties which will be investigated in the late sections.

3 Numerical errors and convergence rate

To illustrate the convergence rate of the SSPC, we choose the following 2-D initial value problem:

$$\frac{\partial^2 u}{\partial x^2}+\frac{\partial^2 u}{\partial z^2}=\frac{1}{c^2}\frac{\partial^2 u}{\partial t^2}, \tag{3.1a}$$

$$u(0,x,z)=\cos\left(-\frac{2\pi f_0}{c}x\cos\theta_0-\frac{2\pi f_0}{c}z\sin\theta_0\right), \tag{3.1b}$$

$$\frac{\partial u(0,x,z)}{\partial t}=-2\pi f_0\sin\left(-\frac{2\pi f_0}{c}x\cos\theta_0-\frac{2\pi f_0}{c}z\sin\theta_0\right), \tag{3.1c}$$

where c is the velocity of the plane wave, θ_0 the incident angle at time $t=0$, f_0 the peak frequency. The exact solution of this initial value problem (3.1) is:

$$u(t,x,z)=\cos\left[2\pi f_0\left(t-\frac{x}{c}\cos\theta_0-\frac{z}{c}\sin\theta_0\right)\right]. \tag{3.2}$$

In the following example, we choose the weighting parameter $\eta=0.7$, the computational region of $0<x\leq 20$ km and $0<z\leq 20$ km, the frequency $f_0=15$ Hz, the acoustic wave velocity $c=4000$ m/sec, the incident angle $\theta_0=\pi/4$, and the wave propagation time $T=1$sec. For the same Courant number $\alpha=0.1$ (defined by $\alpha=c\Delta t/\Delta x$), the errors between the numerical solution u_h computed by the SSPC and the exact solution u are measured in the following L^∞-norm [6]

$$E_{L^\infty}=\|u_h-u\|_{L^\infty}=h^2\max_{i,j}|u^n_{i,j}-u(t_n,x_i,z_j)|, \tag{3.3}$$

where $u^n_{i,j}$ is the numerical solution and $u(t_n,x_i,z_j)$ is the analytic solution of the initial value problem (3.1). The convergence rate [6] is defined as

$$O_{L^\infty}=\log\left(\frac{E^s_{L^\infty}}{E^{s-1}_{L^\infty}}\right)\Big/\log\left(\frac{h^s}{h^{s-1}}\right). \tag{3.4}$$

In Table 1, the first column is the spatial increment, the second column is the numerical errors E_{L^∞} in L^∞-norm, and the third column shows the convergence rate O_{L^∞} of the SSPC for different spatial and temporal increments. We see from Table 1 that the numerical convergence rate of the SSPC increases as dx decreases and is about 3. The convergence rate is dependent mainly on the choice of spatial interval dx or h as defined in Eq. (3.4) (as well as on errors defined in Eq. (3.3)).

Table 1: Convergence rate of the SSPC for the weight parameter of $\eta=0.7$.

Δx	E_{L^∞}	O_{L^∞}
8.00E-2	1.0509E-002	-
4.00E-2	1.6871E-003	2.6390
2.00E-2	2.3269E-004	2.8581
1.00E-2	2.9205E-005	2.9941

4 Stability criteria

The temporal increment, spatial increment, and the wave velocity must satisfy certain relationship to keep numerical calculation stable, which is known as the C-F-L condition. In this section, we derive the stability criteria of the SSPC for 1-D and 2-D cases following the Fourier analysis method of Richtmyer and Morton [19], and Guan and Lu [11].

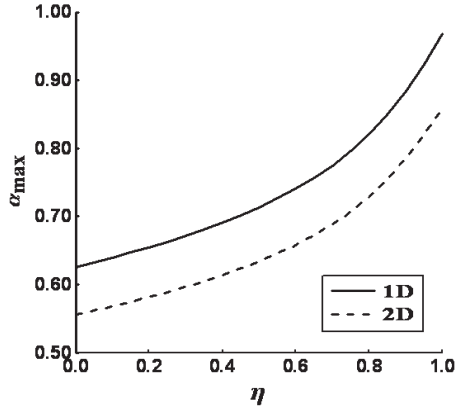

Figure 1: The maximal Courant number of the SSPC for both 1-D and 2-D acoustic cases, which the weight parameter varies from $\eta=0.0$ to $\eta=1.0$.

Through a series of mathematical operations (see Appendix B), we obtain the stability conditions of the SSPC for 1-D and 2-D acoustic homogeneous cases as the weighting parameter varies in $[0,1]$, which are shown in Fig. 1. In Fig. 1, the Courant number α defined by $\alpha=c\Delta t/\Delta x$ increases from 0.626 to 0.968 for the 1-D case and from 0.556 to 0.86 for the 2-D acoustic case as the parameter η changes from 0 to 1. Comparing Fig. 1 and Fig. 1 presented in Chen *et al*. [3] shows that the stability of the SSPC has stronger stability than that of the weighted Runge-Kutta method recently suggested by Chen *et al*. [3]. Table 2 gives different Courant numbers corresponding to different parameter values of η. It illustrates that for different parameter values of η the SSPC has different stability conditions. For example, when $\eta=0.7$, the stability conditions of the SSPC for the acoustic case under the condition of $\Delta x=\Delta z$ are

$$\Delta t\leq\alpha_{\max}\frac{\Delta x}{c}\approx 0.775\frac{\Delta x}{c} \tag{4.1}$$

for the 1-D acoustic case, and

$$\Delta t\leq\alpha_{\max}\frac{\Delta x}{c}\approx 0.609\frac{\Delta x}{c} \tag{4.2}$$

for the 2-D acoustic case, where c denotes the acoustic velocity, Δt the time increment, and Δx and Δz are the space increments in the x- and z-directions, respectively. The maximum value $\alpha_{\max}$ of the Courant number α is given in Appendix B.

Table 2: Approximate maximum Courant numbers of the SSPC for different weight parameters.

η	0.0	0.1	0.2	0.3	0.4	0.5	0.6	0.7	0.8	0.9	1.0
1D	0.626	0.640	0.655	0.672	0.691	0.714	0.741	0.775	0.821	0.884	0.968
2D	0.556	0.568	0.582	0.597	0.614	0.634	0.658	0.689	0.729	0.786	0.860

The stability condition for heterogeneous media cannot be directly determined but could be approximated using a local homogeneous method. Our conjecture is that Eqs. (4.1) and (4.2) are approximately correct for heterogeneous media if the maximum value of the wave velocity c is used.

For the 2-D elastic-wave case that the P- and S-waves couple together with each other, it is difficult to analytically study the stability of the SSPC. However, using many numerical experiments we obtain the approximate stability condition of the SSPC $\Delta t \leq 0.609h/v_p$ with the P-wave velocity v_p under the condition of $\Delta x = \Delta z = h$ when the parameter $\eta = 0.7$. It should be mentioned that the quasi P-wave (qP-wave) velocity varies with elastic-wave propagation directions in anisotropic media, so the velocity v_p in the stability condition should be equal to the maximum qP-wave velocity for the elastic anisotropic case.

5 Numerical dispersion and efficiency

As we know, many numerical methods suffer from numerical dispersion when coarse grids are used or too few samples per wavelength are used, resulting in the limitation of their applications. Sei and Symes [20] observed that the higher the order of the FD schemes, the less numerical dispersion is experienced. However merely by increasing the accuracy of methods cannot effectively suppress the numerical dispersion when too coarse grids are used or models have large velocity contrasts [29]. Another way to deal with the numerical dispersion is to use fine grids, but it will definitely increase computational time and memory. Therefore, to investigate the effect of the numerical dispersion on seismic propagation for different computational parameters is important when a new numerical method is developed and applied to practical seismic wave modeling.

To understand the behavior of the SSPC in suppressing the numerical dispersion, following the methods in the cited references [3,5,29], we derive the numerical dispersion relationship of the SSPC for the 1-D case and compare its numerical results against those of the high-order LWC methods. We also derive 2-D numerical dispersion relationships of the SSPC for different propagation directions to investigate its numerical dispersion anisotropy. The derivation of numerical dispersion relation of the SSPC for both 1-D and 2-D cases are given in detail in Appendix C.

Fig. 2 shows the numerical dispersion curves for the 1-D acoustic case, computed by the SSPC with parameter $\eta = 0.7$ (Fig. 2(a)), fourth-order LWC (Fig. 2(b)), and the eighth-order LWC method (Fig. 2(c)), respectively. From Fig. 2, we can see that for the same Courant number, the SSPC has the least numerical dispersion error compared to the high-order LWC methods. For example, when the Courant number $\alpha = c\Delta t/\Delta x = 0.5$, the maximal deviation of the numerical velocity of the SSPC from the real wave velocity is no greater than 3%, whereas the maximal numerical dispersion errors of the high-order LWC methods are about 15% for the same Courant number.

Fig. 3 shows the numerical dispersion curves of the SSPC (Figs. 3(a) and 3(c)) and the fourth-order staggered-grid FD method (SG) (Figs. 3(b) and 3(d)) for the 2-D case,

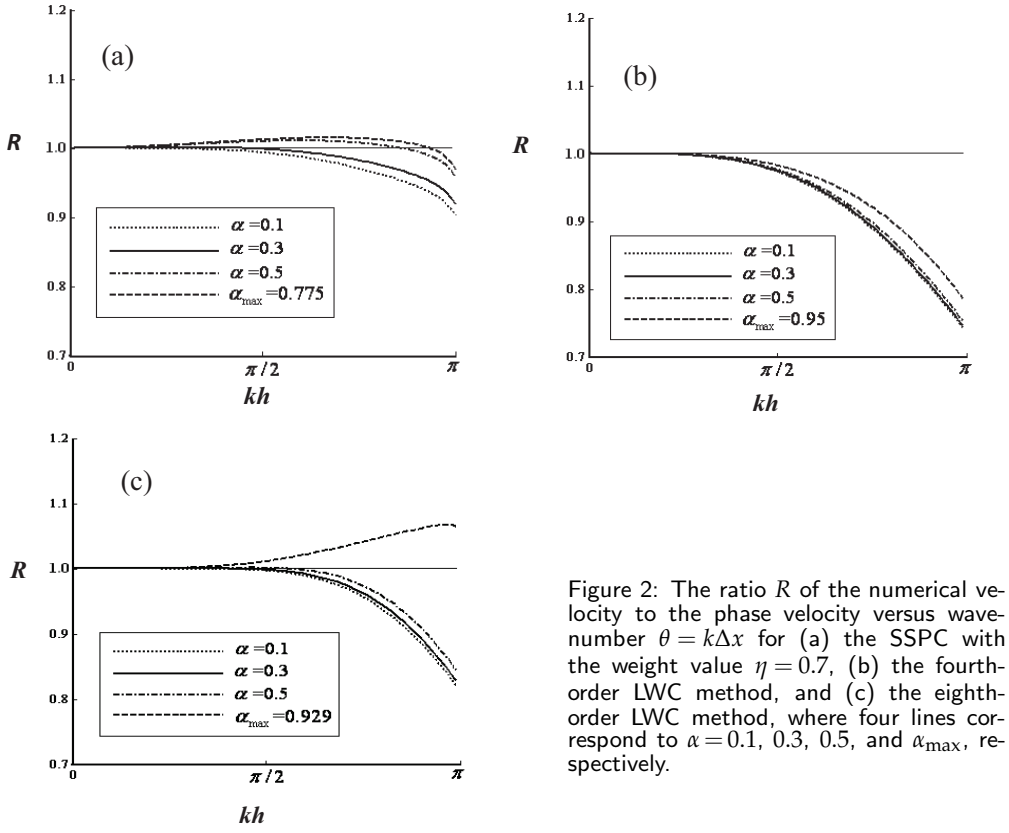

Figure 2: The ratio R of the numerical velocity to the phase velocity versus wavenumber $\theta = k\Delta x$ for (a) the SSPC with the weight value $\eta = 0.7$, (b) the fourth-order LWC method, and (c) the eighth-order LWC method, where four lines correspond to $\alpha = 0.1$, 0.3, 0.5, and $\alpha_{\max}$, respectively.

where four lines correspond to different propagation angles of $\upsilon = 0^\circ$, 15°, 30°, and 45°, and Figs. 3(a)-3(b) and Figs. 3(c)-3(d) correspond to the Courant numbers $\alpha = 0.6$ and $\alpha = 0.1$, respectively. In Fig. 3, for the Courant number of $\alpha = 0.6$, the maximum dispersion error of the SSPC with the weighting parameter $\eta = 0.7$ is no more than 10%, whereas the maximum dispersion error of the SG method reaches about 20%. When $\alpha = 0.1$, the maximal deviation error for the SSPC with $\eta = 0.1$ is no greater than 5% and the maximum dispersion error of the SG method is about 25%. These numerical results demonstrate that the SSPC has smaller numerical dispersion errors than the fourth-order SG method for different weighting parameters and the Courant numbers. Meanwhile, from Figs. 3(a) and 3(c) we can observe that the numerical dispersion curves of the SSPC in different propagation directions are close to each other. It means that the SSPC has small numerical dispersion anisotropy. In contrast, from Figs. 3(b) and 3(d) we can see that the difference of numerical dispersion in different propagation directions is very large, implying that fourth-order SG has larger numerical dispersion anisotropy than that of the SSPC.

In the following, we investigate the numerical dispersion and computational efficiency of the SSPC through wave-field modeling, and compare our method with the fourth-order LWC and the fourth-order SG method. Under this case of our considera-

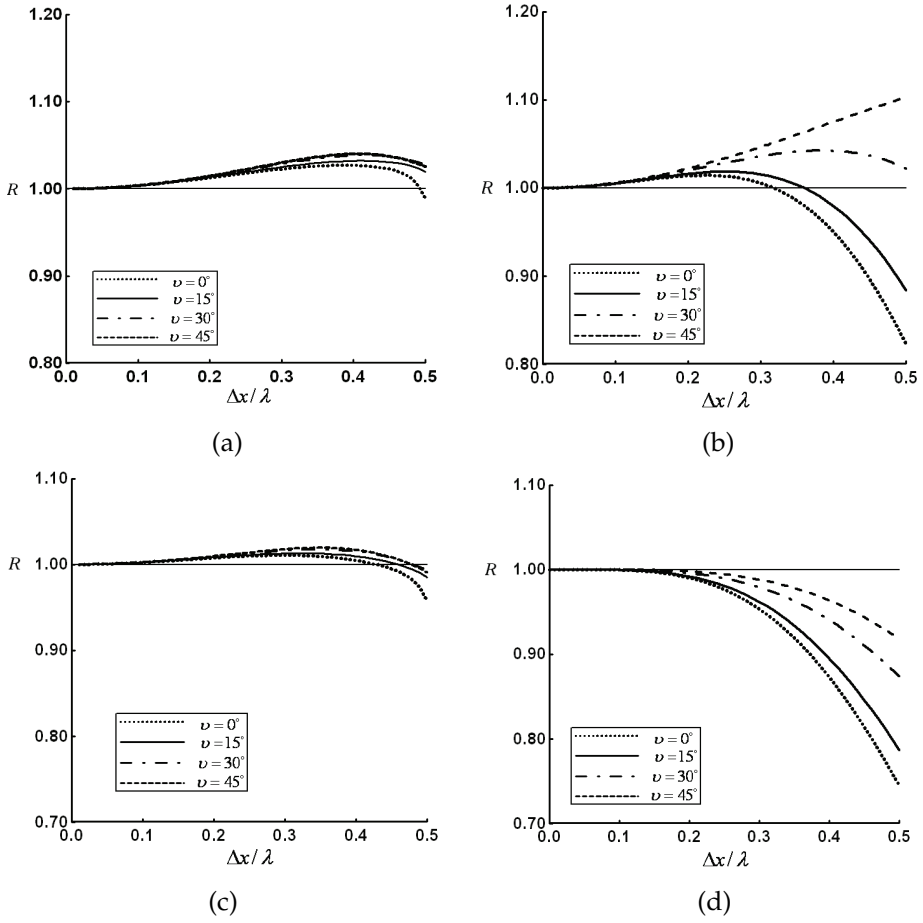

Figure 3: Grid-dispersion curves showing the dependence on the sampling rate S_p defined by $S_p=\Delta x/\lambda$, Δx being the grid spacing and λ the wavelength. The curves correspond to 2-D acoustic wave propagation in 4 azimuths of υ=0°, 15°, 30°, 45°. Figs. 3(a) and 3(b) show the curves for the Courant number α=0.1, computed by the SSPC with weight parameter $\eta=0.1$ and the fourth-order SG, respectively. Analogously, Figures 3c and 3d show the curves computed by the SSPC with $\eta=0.7$ and the fourth-order SG for the Courant number α=0.6.

tion, we choose the following acoustic wave equation

$$\frac{\partial^2 u}{\partial t^2}={c_0}^2\left(\frac{\partial^2 u}{\partial x^2}+\frac{\partial^2 u}{\partial z^2}\right)+f, \tag{5.1}$$

where the force source f which is located at the center of the computational domain, is a Ricker wavelet $f=\sin(2\pi f_0)\exp(-4\pi^2{f_0}^2t^2/16)$ [32] with a peak frequency of $f_0=20$ Hz. The acoustic velocity is $c_0=3000$ m/sec and the computational domain is $0<x\leq 14$ km and $0<z\leq 14$ km.

Fig. 4 shows acoustic wave-field displacement snapshots at $t=2$sec on a coarse grid ($\Delta x=\Delta z=70$m) corresponding to the grid points of $G=c_0/(f_0\cdot\Delta x)=2.14$ per wavelength, generated by the SSPC with $\eta=0.7$ (Fig. 4(a)), fourth-order LWC (Fig. 4(b)), and

the fourth-order SG (Fig. 4(c)), respectively. Note that the source is an explosive source and excites equal energy in all directions and also in all examples in this paper, wave-field displacements are shown unless stated otherwise. In Fig. 4, the wave fronts of seismic propagation simulated by the three methods at the same time are nearly identical. However, Fig. 4(a) generated by the SSPC shows no visible numerical dispersion on the coarse grid ($\Delta x=\Delta z=70$m), whereas Figs. 4(b) and 4(c) generated by the fourth-order LWC and fourth-order SG methods show serious numerical dispersion. To eliminate the numerical dispersion caused by the fourth-order LWC and fourth-order SG methods, we use the finer grids. For instance, for these parameters used in the numerical experiment we have to use the fine grids of $\Delta x=\Delta z=10$m (corresponding to $G\approx 15$) for the fourth-order LWC and $\Delta x=\Delta z=8$m ($G\approx 18.8$) for the fourth-order SG method to eliminate the numerical dispersion. Fig. 5 shows the wave-field snapshots at $t=2$sec on the fine grids for the same courant number $\alpha=0.21$, generated by the fourth-order LWC ($\Delta x=\Delta z=10$m, $G\approx 15$, Fig. 5(a)) and the fourth-order SG ($\Delta x=\Delta z=8m$, $G\approx 18.8$, Fig. 5(b)).

Comparing Fig. 4(a) with Fig. 5, we can see that the SSPC on the coarse grid ($\Delta x=\Delta z=70$m) can provide the same numerical accuracy as those of the fourth-order LWC and the fourth-order SG method on the fine grids. Therefore, the computational cost of the SSPC on the coarse grid is much less than those of the other two methods on the fine grids. For example, it took the SSPC about 1.65 min to generate Fig. 4(a), whereas fourth-order LWC method and the fourth-order SG method took about 116.2 min and 47.3 min to generate Figs. 5(a) and 5(b), respectively. It means that the computational speed of the SSPC is roughly 70 times of the fourth-order LWC and about 29 times of the fourth-order SG method to achieve the same accuracy of the SSPC. The computations of Figs. 4 and 5 were performed on a PC with 2GB memory and 2.66 GHz CPU.

Meanwhile, the memory required for computation in the SSPC is also different from those of the fourth-order LWC and the fourth-order SG. The SSPC needs twenty-four arrays to store wave displacements $u_{i,j}^{n+1}$ and $u_{i,j}^{n}$, the particle-velocity w_{ij}^{n+1} and w_{ij}^{n}, and their gradients at each spatial grid point, and the number of grid points for each array is 201×201 on a coarse grid for generating Fig. 4(a). The fourth-order LWC needs only three arrays to store the wave displacements $u_{i,j}^{n-1}$, $u_{i,j}^{n}$, and $u_{i,j}^{n+1}$ at each grid point, and the fourth-order SG method needs five arrays to store both the velocity and two stresses at each grid point, but the number of grid points on the fine grid for generating Figs. 5(a) and 5(b) increases to 1401×1401 for the fourth-order LWC method and to 1751×1751 for the fourth-order SG, respectively. It indicates that the memory of the SSPC requires about 16% of the fourth-order LWC and 6% of the fourth-order SG.

To further demonstrate the computational accuracy and the validity of the SSPC, we compare the waveforms generated by the SSPC with the weighting parameter $\eta=0.7$ and the Cagniard-de Hoop method in Aki and Richards [1] for acoustic wave modeling. In the numerical experiment, we choose the wave velocity $c=4000$ m/sec, the spatial increment is $\Delta x=\Delta z=60$m, and the source time function is

$$f=-5.76{f_0}^2[1-16(0.6f_0t-1)^2]\exp[-8(0.6f_0t-1)^2]. \tag{5.2}$$

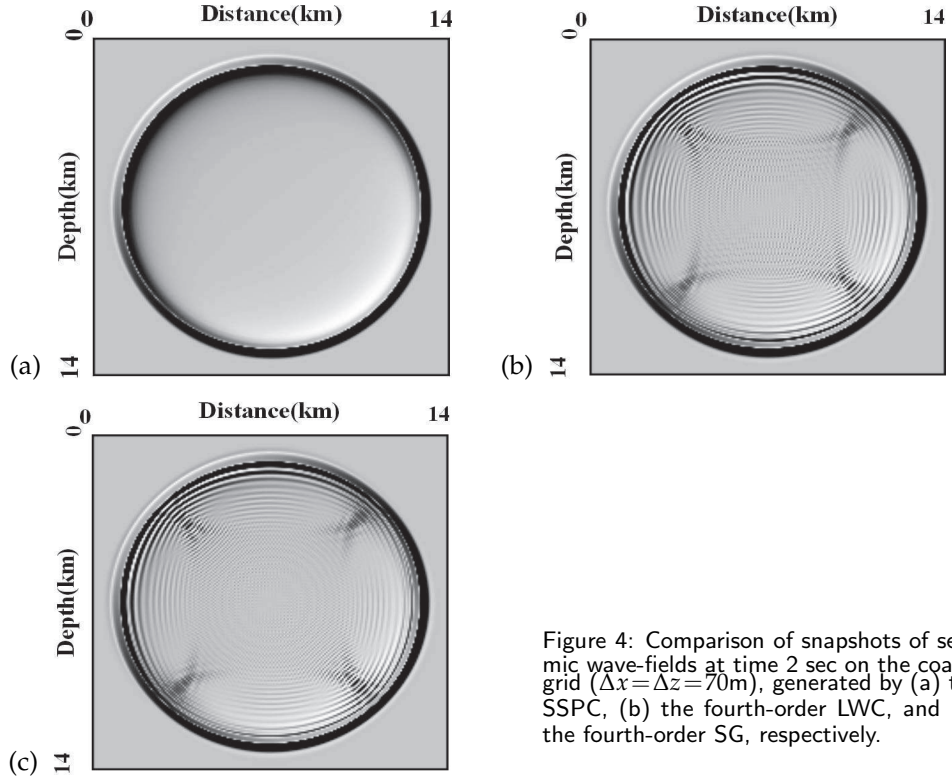

Figure 4: Comparison of snapshots of seismic wave-fields at time 2 sec on the coarse grid ($\Delta x = \Delta z = 70$m), generated by (a) the SSPC, (b) the fourth-order LWC, and (c) the fourth-order SG, respectively.

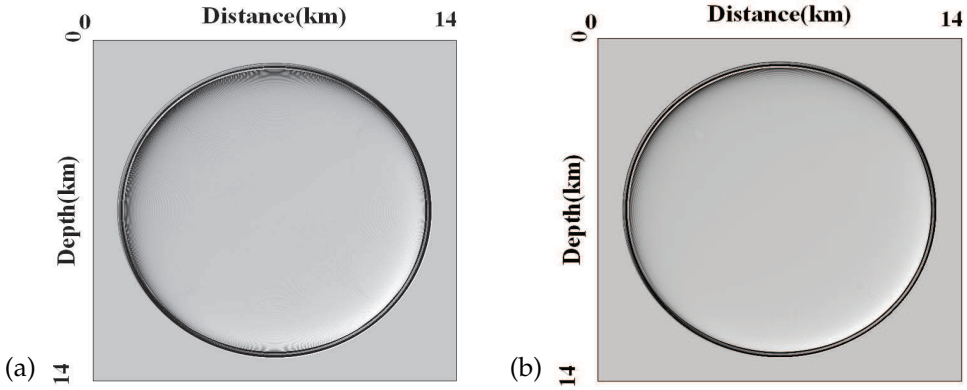

Figure 5: Snapshots of seismic wave fields at time 2 sec on the fine grids, generated by (a) the fourth-order LWC ($\Delta x = \Delta z = 10$m) and (b) the fourth-order SG ($\Delta x = \Delta z = 8$m), respectively.

The source is located at the center of the computational domain with a central frequency $f_0 = 15$ Hz. The receiver is 3km away from the source along the z-axis.

Fig. 6 shows the waveforms of the analytic solution (solid lines) and the numerical solutions on the coarse grid ($\Delta x = \Delta z = 60$m), generated by the SSPC, fourth-order LWC, and the fourth-order SG, respectively. Fig 6(a) shows that the waveforms calculated by

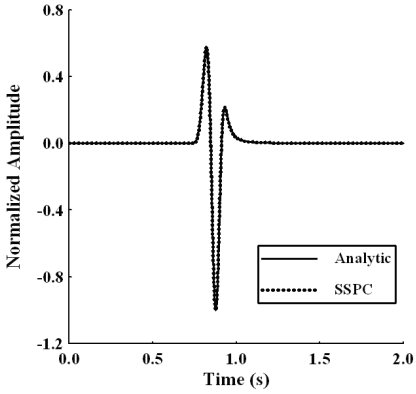

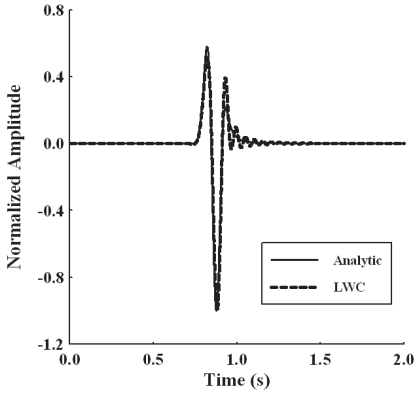

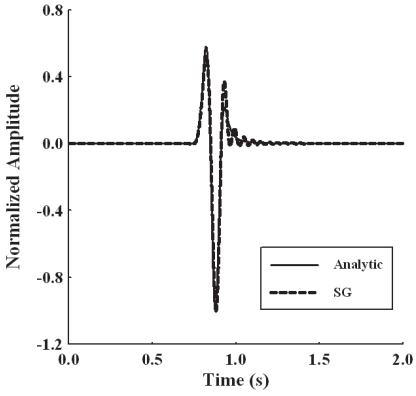

Figure 6: Comparison of numerical waveforms on the coarse grid ($\Delta x=\Delta z=60$m) with the analytic solution (solid line) for the homogenous medium case, generated by (a) the SSPC, (b) the fourth-order LWC method, and (c) the fourth-order SG. Especially, Fig. 6(a) shows the excellent coincidence between the numerical solution (dotted line) and the exact analytic solution (solid line).

the SSPC (dotted line) and the Cagniard-de Hoop method (solid line) are in good overall agreement even on the coarse grid ($\Delta x=\Delta z=60$m). In contrast, the results in Figs. 6(b) and 6(c), calculated by the fourth-order LWC and the SG methods, respectively, show serious numerical dispersion following the peak wave as contrasted to the analytic solution (solid line). It illustrates that the SSPC is accurate in wave-field modeling for the acoustic propagation modeling and it can provide very accurate results even when coarse grids are chosen.

To test the validity of the SSPC for multi-layer medium models with large velocity contrasts in seismic propagation modeling, we first choose a two-layer acoustic model with the velocity 2.5 km/sec in the upper layer medium and 4.5 km/sec in the lower layer medium. The computational region is $0<x\leq 4$ km and $0<z\leq 4$ km, and the depth of the horizontal inner interface is at $z=2.2$ km. The source is the same as that used in the acoustic model, located at the coordinate (2 km, 1.6 km) with a peak frequency of $f_0=40$ Hz. A receiver is located at R(2.4 km, 1.2 km). The spatial increment is 10 m and the time step is $\Delta t=1\times 10^{-4}$sec. Fig. 7 shows the comparison of waveforms computed by the

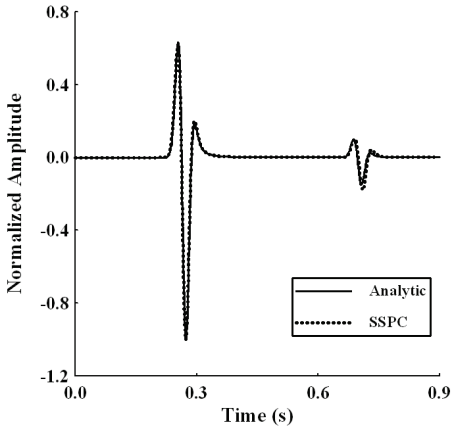

Figure 7: Comparison of the numerical result (dotted line) computed by the SSPC for the higher frequency (f_0=40Hz) on the medium grid ($\Delta x=\Delta z$=10m) with the analytic solution (solid line) for the two-layer acoustic model with a strong interface.

SSPC with the weighting parameter $\eta = 0.7$ and the analytic solution computed by the Cagniard-de Hoop method [1]. From Fig. 7 we can see that the waveform (dotted line) generated by the SSPC is nearly the same as the analytic solution (solid line).

6 Numerical examples

To test the accuracy and validity of the SSPC in modeling wave propagation for complex geological cases, in this section, we use the SSPC to model seismic wave propagating in three different media including a transversely isotropic medium with the vertical symmetry axis (VTI), two-layer elastic medium, and a heterogeneous medium. For comparison, we present these wavefield results of the high-order LWC methods such as fourth-order and eighth-order LWC methods. Meanwhile, in order to confirm that the SSPC is an improved version of our previous method, we also show wavefield snapshots computed by the IRK-DSK [31].

2D homogeneous VTI model

In this example, we consider the following elastic wave equation in a 2D homogeneous VTI medium:

$$\begin{cases} \rho\dfrac{\partial^2 u_1}{\partial t^2} = c_{11}\dfrac{\partial^2 u_1}{\partial x^2} + (c_{13}+c_{44})\dfrac{\partial^2 u_3}{\partial x \partial z} + c_{44}\dfrac{\partial^2 u_1}{\partial z^2} + f_1, \\ \rho\dfrac{\partial^2 u_2}{\partial t^2} = c_{66}\dfrac{\partial^2 u_2}{\partial x^2} + c_{44}\dfrac{\partial^2 u_2}{\partial z^2} + f_2, \\ \rho\dfrac{\partial^2 u_3}{\partial t^2} = (c_{13}+c_{44})\dfrac{\partial^2 u_1}{\partial x \partial z} + c_{44}\dfrac{\partial^2 u_3}{\partial x^2} + c_{33}\dfrac{\partial^2 u_3}{\partial z^2} + f_3, \end{cases} \tag{6.1}$$

where u_1, u_2, and u_3 denote the displacements in the x-, y-, and z-directions, respectively. c_{11}, c_{13}, c_{33}, c_{44}, and c_{66} are elastic constants, ρ the medium density, f_1, f_2, and f_3 the force source components in the x-, y-, and z-directions, respectively.

In this experiment, We choose the elastic constants $c_{11}=32.5$GPa, $c_{13}=7.5$GPa, $c_{33}=19.5$GPa, $c_{44}=6.5$GPa, and $c_{66}=9.75$GPa, the density $\rho=2$ g/cm^3. The explosive source is a Ricker wavelet with a peak frequency of $f_0=15$Hz and is located at the center of the

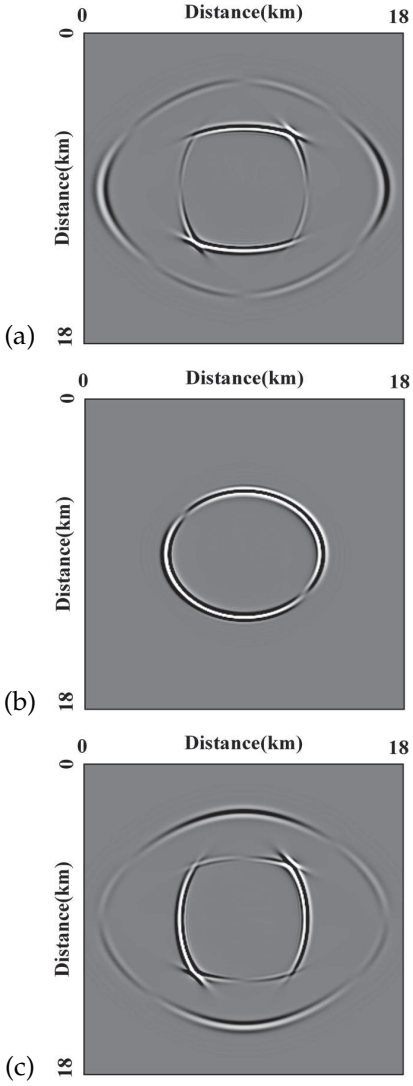

Figure 8: Wave-field snapshots for the three components of the displacement at time $t=2.5$sec in the VTI medium, generated by the SSPC, for (a) u_1 component, (b) u_2 component, and (c) u_3 component.

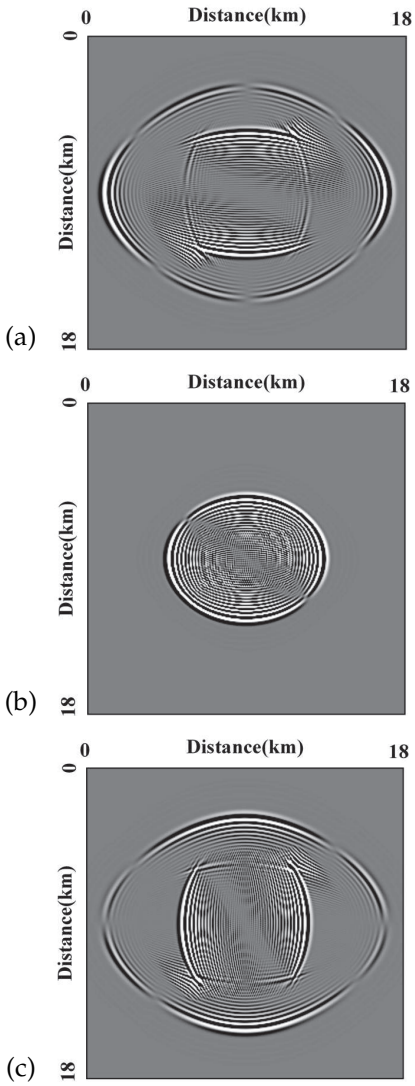

Figure 9: Wave-field snapshots for the three components at time $t=2.5$sec in the VTI medium, generated by the fourth-order LWC, for (a) u_1 component, (b) u_2 component, and (c) u_3 component.

computational domain. The source function is the same as in Eq. (5.2). The spatial increments are $\Delta x=\Delta z=60$m, resulting in the number of grid points per minimal wavelength is about $G=2$, which is a minimal spatial sampling point number in a wavelength in numerical simulations. The grid points is 301×301, corresponding to the computational domain of $0<x\leq18$km and $0<z\leq18$km.

Figs. 8 and 9 are the wave-field snapshots for the three displacement-components at the time $t=2.5$sec, generated by the SSPC with the weight value of $\eta=0.1$ (Fig. 8) and the fourth-order LWC (Fig. 9), respectively. From Figs. 8 and 9, we can see that the snapshots generated by the SSPC are very clear and no visible numerical dispersion, whereas the fourth-order LWC suffers from serious numerical dispersion on the coarse grids ($\Delta x=\Delta z=60$m) (see Fig. 9). We can also see the difference of arrival time of the quasi-SV (qSV) wave and quasi-SH (qSH) wave through the comparison of the qSV waves shown in Figs. 8(a) or 8(c) and the qSH wave shown in Fig. 8(b). To observe more clearly the difference of arrival time of the shear waves shown in different components of the wave displacement, we present a snapshot shown in Fig. 10, which is actually a stack of Fig. 8(b) and Fig. 8(c). From Fig. 10 we see clear shear wave splitting — differences in wave speeds between *qSH* and *qSV* waves.

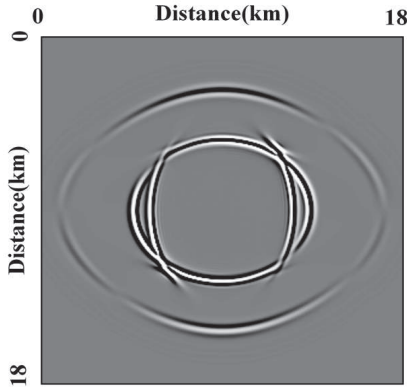

Figure 10: A stack snapshot of the quasi-SH wave-field shown in Fig. 8(b) and the quasi-SV wave-field shown in Fig. 8(c). Clear shear-wave splitting in the 2-D VTI medium is observed from Fig. 10 through using the stack of two wave fields of u_2 and u_3 components.

Two-layer elastic model

In this experiment, we first choose a two-layer medium model with a strong interface to test the validity of the SSPC for the elastic case through comparing the waveforms computed by the SSPC and the eighth-order LWC used widely in seismic simulations. The computational region is $0<x\leq20$ km and $0<z\leq20$ km, and the depth of the horizontal inner interface is $z=10.8$ km. The P- and S-wave velocities are 4.014 km/s and 2.472 km/s in the upper layer, and 5.06 km/s and 3.162 km/s in the lower layer, respectively.

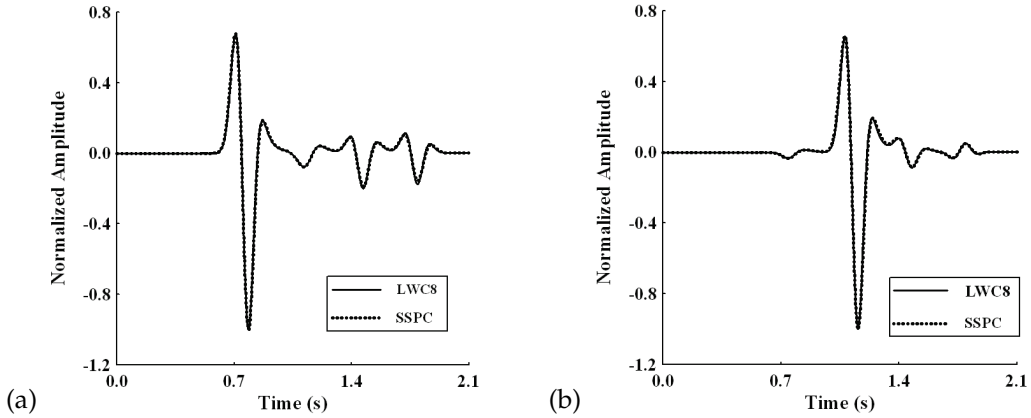

Figure 11: Comparison of waveforms in the two-layer elastic medium, generated by the SSPC and the eighth-order LWC on the fine grid ($\Delta x=\Delta z=10$m) for (a) the horizontal component u_1 and (b) the vertical component u_3.

The source is located at the coordinate (10 km, 9.2km) and its time variable function is the same as in Eq. (5.2).

Fig. 11 are the waveforms of the horizontal component (u_1) (Fig. 11(a)) and vertical component (u_3) (Fig. 11(b)) at receiver R(7.6 km, 9.2km), generated by the SSPC and the eighth-order LWC method on the fine grid ($\Delta x=\Delta z=10$m). Fig. 11 shows that the waveforms calculated by the SSPC and the eighth-order LWC method are in good agreement. Because Dablain [5] in his study has demonstrated that the eighth-order LWC on fine grids can provide accurate numerical results which are similar to the analytic solution and equivalent with the pseudospectral method. It implies that the SSPC can provide accurate seismic modeling result for the two-layer elastic case. In the experiment, the absorbing boundary condition presented by Yang *et al.* [28] is used.

Next, we investigate the effectiveness of the SSPC in suppressing the numerical dispersion for the two-layer elastic model with large velocity contrasts between adjacent layers when using large space steps, and compare SSPC against the high-order LWC [5] and the IRK-DSM [31]. In this example, the Lamé constants and density in the upper layer medium are $\lambda_1=5.0$GPa, $\mu_1=8.0$GPa, and $\rho_1=1.8$g/cm^3, resulting in the P- and S-wave velocities of 3.73 km/s and 2.11 km/s, and the Lamé constants and density in the lower layer medium are $\lambda_2=15.0$GPa, $\mu_2=25.0$GPa, and $\rho_2=2.0$g/cm^3, corresponding to the P- and S-wave velocities of 5.70 km/s and 3.54 km/s. The spatial increments and the time step are $\Delta x=\Delta z=40$m and $\Delta t=2\times10^{-3}$sec, respectively. The source function is the same as in Eq. (5.2) and a peak frequency of the source is $f_0=18$Hz. The other parameters such as the computational region and locations of source and horizontal inner interface are the same as those used in the previous two-layer elastic model.

Figs. 12 to 14 show the wave-field snapshots for the horizontal displacements (u_1) (Figs. 12(a), 13(a), 14(a)) and the vertical displacements (u_3) (Figs. 12(b), 13(b), 14(b)) at time $t=2$ sec for the two-layer elastic medium model with velocity contrasts of 1.68 times

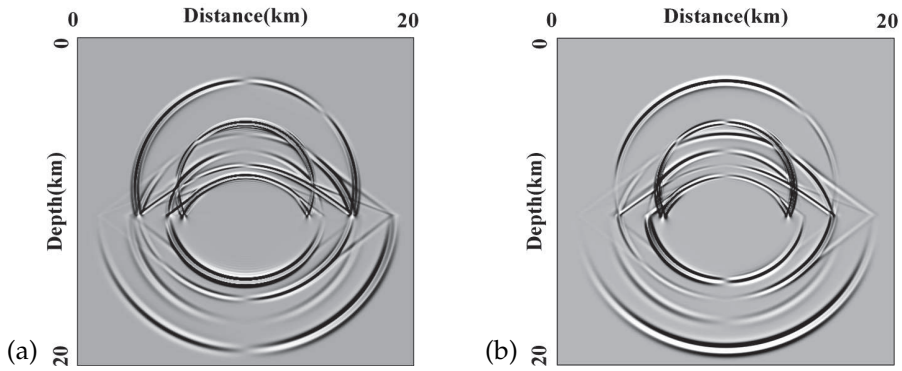

Figure 12: Snapshots of elastic-wave fields at time 2 sec on a coarse gird ($\Delta x = \Delta z = 40$m) for the two-layer elastic model, generated by the SSPC for (a) the horizontal component u_1 and (b) the vertical component u_3.

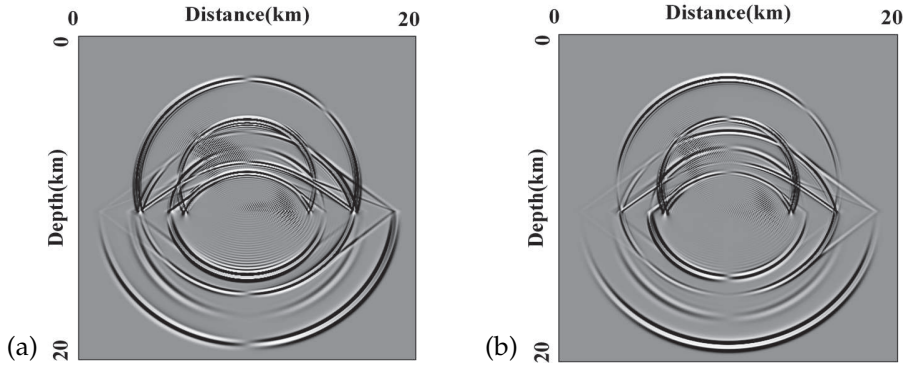

Figure 13: Snapshots of elastic-wave fields at time 2 sec on a coarse gird ($\Delta x = \Delta z = 40$m) for the two-layer elastic model, generated by the IRK-DSM [31] for (a) the horizontal component u_1 and (b) the vertical component u_3.

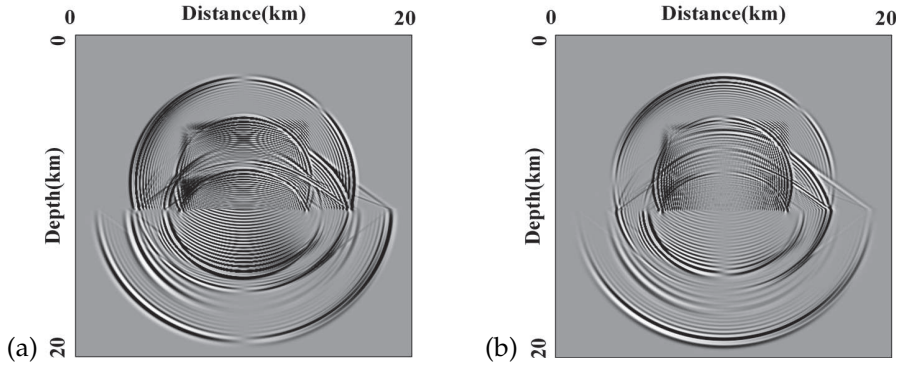

Figure 14: Snapshots of elastic-wave fields at time 2 sec on a coarse gird ($\Delta x = \Delta z = 40$m) for the two-layer elastic model, generated by the fourth-order LWC [5] for (a) the horizontal component u_1 and (b) the vertical component u_3.

between upper and lower layers, generated by the SSPC with the weight value of $\eta=0.7$, IRK-DSM, and the fourth-order LWC on the grids of $\Delta x=\Delta z=40$m. From Fig. 12 computed by the SSPC, we can observe that numerous phases such as direct P-wave, direct S-wave, and their reflected, transmitted, and converted phases from the inner interface are very clear, and shows no visible numerical dispersions. However, the snapshots generated by the IRK-DSM (Fig. 13) show small numerical dispersion, and the fourth-order LWC method suffers from serious numerical dispersion (Fig. 14). It demonstrates that the SSPC method is very effective in suppressing numerical dispersion for two-layer elastic model with large velocity contrasts even on the grids ($\Delta x=\Delta z=40$m). The comparison of Figs. 12 and 13 also shows that the SSPC further increases the ability of suppressing the numerical dispersion as compared with the original IRK-DSM [31]. In other words, it confirms that the SSPC is in fact an improved version or an extension of the IRK-DSM.

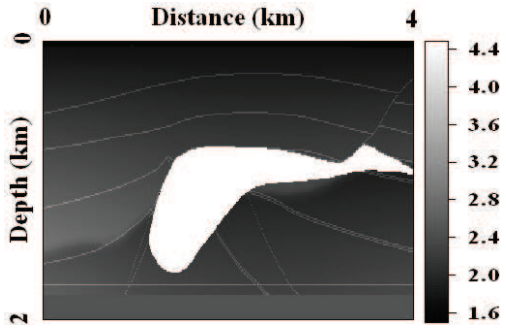

Figure 15: The SEG/EAGE salt model with the minimum acoustic velocity of 1500 m/s and maximum velocity of 4482 m/s.

2-D SEG/EAGE salt-dome model

As a last example we choose the 2-D standard SEG/EAGE salt model shown in Fig. 15 for the case of the spatial steps $\Delta x=\Delta z=10$m, which shows the acoustic-velocity structure and the velocity varies from 1500 m/s to 4482 m/s. The number of grid points is 401×201, different spatial and time increments, given in Table 3, are chosen to test the efficiency of the SSPC with the weight value $\eta=0.1$ for the SEG model. The source with a peak frequency of $f_0=20$Hz is located on the surface, and the time variation of the source function is the same as in Eq. (5.2).

Table 3: CPU time of the SSPC for different spatial and temporal increments ($\Delta x=\Delta z=h$), and different computational domains. Synthetic seismograms are shown in Fig. 16.

h (m)	Δt(sec)	Computational domain	Record length (sec)	CPU time (min)
20	0.0024	$0\le\Delta x\le8$km, $0\le\Delta z\le4$km	4	13
50	0.005	$0\le\Delta x\le20$km, $0\le\Delta z\le10$km	9	14
200	0.024	$0\le\Delta x\le80$km, $0\le\Delta z\le40$km	35	11.7

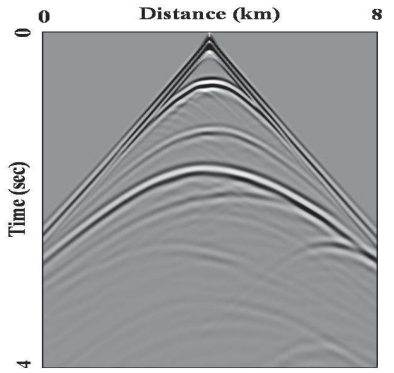

(a) $\Delta x=\Delta z=20$m and $\Delta t=0.0024$ sec

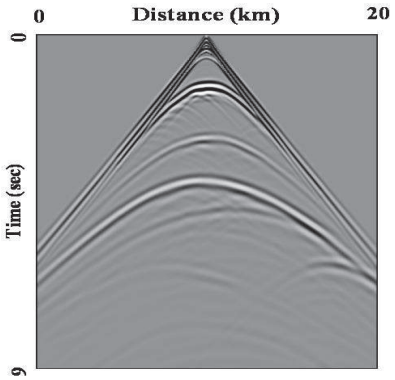

(b) $\Delta x=\Delta z=50$m and $\Delta t=0.005$ sec

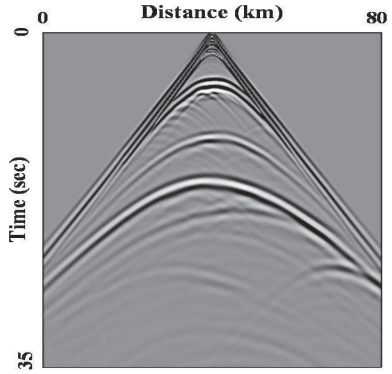

(c) $\Delta x=\Delta z=200$m and $\Delta t=0.024$ sec

Figure 16: Synthetic seismograms for different spatial increments and different spatial and temporal steps for the SEG/EAGE salt model, generated by the SSPC with the weight value of $\eta=0.1$. The spatial parameters used in this example and computational CPU time are listed in Table 2.

Fig. 16 shows the synthetic records on the surface, generated by the SSPC for different model sizes and grid intervals (Table 3), using the decoupling 2-time absorbing boundary condition of Yang *et al.* [28]. The seismograms are all clean and have no visible numerical dispersion even for coarser grid spacing of up to 200 m, thus confirming that the SSPC produces no visible numerical dispersion for large spatial intervals and time increments in heterogeneous media. The numerical results from the SEG/EAGE salt model also show that the SSPC has good performance even if the velocity varies from 1500 m/s to 4482 m/s. On a PC with 2GB memory and 2.66 GHz CPU, Figs. 16(a), 16(b), and 16(c) generated by the SSPC, which correspond to computational domains of 8 km$\times$4 km, 20 km$\times$10 km and 80 km$\times$40 km (Table 3), consume rough times of 13 min, 14 min and 11.7 min, respectively, so that the proposed method can be used to simulate large-scale seismic modeling using large spatial and time steps.

Besides, in the experiment for the SEG/EAGE salt model with strong interfaces, we find that the SSPC performs better in suppressing the numerical dispersion when the weight parameter η is relatively small. For example, when the parameter η is equal to or smaller than 0.1 the SSPC is quite effective.

7 Discussion and conclusions

In this paper, we propose a strong stability-preserving predictor-corrector method (SSPC) to solve the acoustic- and elastic- wave equations, which is based on both the implicit Runge-Kutta method and a strong stability-preserving explicit scheme. Computations of numerical errors for different spatial steps illustrate that the convergence rate of SSPC is about 3. The accuracy and validity of the SSPC are confirmed through comparisons of numerical results computed by the SSPC and the analytic results computed by the Cagniard-de Hoop method for the acoustic-wave model and the two-layer acoustic model with a strong interface. Meanwhile, the comparison of the elastic waveforms, computed by the SSPC and the eighth-order LWC on fine grids, shows that the SSPC method can provide accurate wavefield results for the complex elastic medium case.

Through applying the idea of the strong stability-preserving m-step Runge-Kutta method [22, 23] to the implicit equations (2.7b) and (2.7c), we can explicitly compute the slopes $K_{i,j}^n$ and $\overline{K}_{i,j}^n$ using Eqs. (2.8) and (2.11). In other words, we introduce a weight parameter η into the m-step predictor-corrector method to compute the slopes $K_{i,j}^n$ and $\overline{K}_{i,j}^n$ at time t_n and the grid point (i,j). The introduction of the weight parameter η improves the ability of suppressing the numerical dispersion as compared with the so-called IRK-DSM [31], which is confirmed in several numerical experiments (see Figs. 12, 13). Meanwhile, numerical dispersion analyses for 1-D and 2-D acoustic cases show that the numerical dispersion error of the SSPC is smaller than those of the fourth-order LWC, eighth-order LWC, and the fourth-order staggered-grid (SG) methods. Seismic modeling results for homogeneous and heterogeneous cases further demonstrate that the new SSPC method has more strong ability of suppressing numerical dispersion than the high-order FD methods such as high-order LWC and fourth-order SG methods. The SSPC can also provide clean wave fields in anisotropic media and the difference of arrival times of qSH- and qSV-waves in the VTI medium (see Figs. 8, 10).

Our dispersion analyses and several numerical examples, including the 2-D homogeneous VTI model, two-layer acoustic and elastic models, and the 2-D SEG/EAGE salt model, show that the main advantage of the SSPC is its powerful ability in suppressing numerical dispersion in heterogeneous and anisotropic media even when very coarse grids are used or models have large velocity contrasts between adjacent layers. It implies that the SSPC can decrease the CPU costs and reduce memory using larger spatial grid steps and further resulting in using larger time increments under the condition of keeping the numerical calculation stable. As shown in the acoustic wave-field modeling, the computational speed of the SSPC is roughly 70 times of the fourth-order LWC and about 29 times of the fourth-order staggered-grid FD method computed on a fine grid under the same Courant number to achieve the same accuracy of the SSPC, and the memory of the SSPC requires only roughly 16% of the fourth-order LWC method and about 6% of the fourth-order staggered-grid method, respectively. For its effectiveness of suppressing numerical dispersion in anisotropic and heterogeneous media, we initiate

complicated applications of the SSPC including large-scale wave propagation modeling, reverse time migration, and inversion based on the wave equations.

Acknowledgments

This work was supported by the National Science Foundation of China under the Distinguished Young Scholars (Grant No. 40725012) and the National Natural Science Foundation of China (Grant No. 41074073). We would like to thank two anonymous reviewers for their detailed and constructive comments that have improved the readability of this paper.

A Approximations of spatial differential operators

To solve Eq. (2.6), we first need to discretize the spatial differential operator $\overline{L}$ included in Eq. (2.6) through using a difference operator. In our present study, we apply the nearly-analytic discrete operators suggested by Yang *et al.* [30,31] to approximate $\overline{L}$. For convenience, we list these approximation formulae used in the SSPC method as follows

$$\partial_{2x}V_{i,j}^n=\frac{2}{\Delta x^2}\delta_x^2V_{i,j}^n-\frac{1}{2\Delta x}(E_x^1-E_x^{-1})\partial_xV_{i,j}^n, \tag{A.1}$$

$$\partial_{2z}V_{i,j}^n=\frac{2}{\Delta z^2}\delta_z^2V_{i,j}^n-\frac{1}{2\Delta z}(E_z^1-E_z^{-1})\partial_zV_{i,j}^n, \tag{A.2}$$

$$\begin{aligned}\partial_{xz}V_{i,j}^n=&\frac{1}{2\Delta x}(E_x^1-E_x^{-1})\partial_zV_{i,j}^n+\frac{1}{2\Delta z}(E_z^1-E_z^{-1})\partial_xV_{i,j}^n\\&-\frac{1}{4\Delta x\Delta z}(E_x^1E_z^1-E_x^1E_z^{-1}-E_x^{-1}E_z^1+E_x^{-1}E_z^{-1})V_{i,j}^n,\end{aligned} \tag{A.3}$$

$$\partial_{3x}V_{i,j}^n=\frac{15}{2\Delta x^3}(E_x^1-E_x^{-1})V_{i,j}^n-\frac{3}{2\Delta x^2}(E_x^1+8I+E_x^{-1})\partial_xV_{i,j}^n, \tag{A.4}$$

$$\partial_{3z}V_{i,j}^n=\frac{15}{2\Delta z^3}(E_z^1-E_z^{-1})V_{i,j}^n-\frac{3}{2\Delta z^2}(E_z^1+8I+E_z^{-1})\partial_zV_{i,j}^n, \tag{A.5}$$

$$\begin{aligned}\partial_{2xz}V_{i,j}^n=&\frac{1}{4\Delta x^2\Delta z}(5E_x^1E_z^1-5E_x^{-1}E_z^{-1}+E_x^1E_z^{-1}-E_x^{-1}E_z^1-4E_z^1+4E_z^{-1}-6E_x^1+6E_x^{-1})V_{i,j}^n\\&+\frac{1}{2\Delta x\Delta z}(-E_x^1E_z^1-E_x^{-1}E_z^{-1}+E_x^1+E_x^{-1}-2\delta_z^2)\partial_xV_{i,j}^n+\frac{1}{\Delta x^2}\delta_x^2(\partial_zV_{i,j}^n),\end{aligned} \tag{A.6}$$

$$\begin{aligned}\partial_{x2z}V_{i,j}^n=&\frac{1}{4\Delta x^2\Delta z}(5E_x^1E_z^1-5E_x^{-1}E_z^{-1}-E_x^1E_z^{-1}+E_x^{-1}E_z^1-4E_x^1+4E_x^{-1}-6E_z^1+6E_z^{-1})V_{i,j}^n\\&+\frac{1}{2\Delta x\Delta z}(-E_x^1E_z^1-E_x^{-1}E_z^{-1}+E_z^1+E_z^{-1}-2\delta_x^2)\partial_zV_{i,j}^n+\frac{1}{\Delta z^2}\delta_z^2(\partial_xV_{i,j}^n),\end{aligned} \tag{A.7}$$

where the vector V is defined by $V=(U,W)^T$, with U and W are the displacement and the particle-velocity, respectively. The difference operators included in Eqs. (A.1)-(A.7)

are defined by $\delta_z^2 V_{i,j}^n = V_{i,j+1}^n - 2V_{i,j}^n + V_{i,j-1}^n$, $E_z^1 V_{i,j}^n = V_{i,j+1}^n$ and $E_z^{-1} V_{i,j}^n = V_{i,j-1}^n$ in the z-direction. The difference operators δ_x^2, E_x^1, and E_x^{-1} in the x-direction can be similarly defined. Besides, the symbols $V_{i,j}^n$, $\partial_x V_{i,j}^n$, $\partial_z V_{i,j}^n$, and $\partial_{mxkz} V_{i,j}^n$ denote $V(i\Delta x, j\Delta z, n\Delta t)$, $\frac{\partial}{\partial x} V(i\Delta x, j\Delta z, n\Delta t)$, $\frac{\partial}{\partial z} V(i\Delta x, j\Delta z, n\Delta t)$, and $(\partial^{m+k} V / \partial x^m \partial z^k)_{i,j}^n$, respectively.

B Derivation of stability criteria

1-D homogeneous case

For the 1-D case, these approximate formulae for computing high-order space derivatives (A.1) and (A.4) can be degenerated into the following formulae

$$\partial_{2x} V_j^n = \frac{2}{\Delta x^2} \delta_x^2 V_j^n - \frac{1}{2\Delta x} \left(E_x^1 - E_x^{-1} \right) \partial_x V_j^n, \tag{B.1}$$

$$\partial_{3x} V_j^n = \frac{15}{2\Delta x^3} \left(E_x^1 - E_x^{-1} \right) V_j^n - \frac{3}{2\Delta x^2} \left(E_x^1 + 8I + E_x^{-1} \right) \partial_x V_j^n. \tag{B.2}$$

To obtain the stability condition of the SSPC, we consider the harmonic solution of Eq. (2.7a) with Eqs. (2.8) and (2.11) for the 1-D case. Substituting the following solution

$$\overline{V}_j^n = \begin{pmatrix} u^n \\ w^n \\ \partial_x u^n \\ \partial_x w^n \end{pmatrix} \exp(i(kjh)), \tag{B.3}$$

into Eqs. (2.7a), (2.8) and (2.11) with relations (B.1) and (B.2), we can obtain the following equation

$$\overline{V}^{n+1} = G \overline{V}^n, \tag{B.4}$$

where G is the amplification matrix.

Let G^* denote the conjugate transpose matrix of G, following the Fourier analyses [11, 19], we know that the SSPC with the amplification matrix G is stable if $\rho(G^* \cdot G) \leq 1$ is satisfied. For a fixed weight parameter $\eta = 0.7$, we can obtain the following stability condition, deriving from the condition of $\rho(G^* \cdot G) \leq 1$,

$$\alpha \leq \alpha_{\max} \leq 0.775, \tag{B.5}$$

or

$$\Delta t \leq \alpha_{\max} \frac{h}{c_0} \approx 0.775 \frac{h}{c_0}, \tag{B.6}$$

where $\alpha_{\max}$ denotes the maximum Courant number that keeps the numerical calculation stable.

2-D homogeneous case

For the 2-D problem, we consider the case of $\Delta x=\Delta z=h$. Following the same steps as discussed in the 1-D case, we can obtain the stability condition of the SSPC with the weight value of $\eta=0.7$ as follows

$$\Delta t\leq\alpha_{\max}\frac{h}{c_0}\approx 0.609\frac{h}{c_0}.$$

For other weight parameter (η) values, we also present some stability conditions of the SSPC, listed in Table 2.

C Numerical dispersion relations

1-D homogeneous case

To investigate the numerical dispersion error of the SSPC, we derive the numerical dispersion relation of the SSPC for the 1-D case. Following the dispersion analysis methods presented in Dablain [5] and Yang *et al.* [29], we consider the harmonic solution of Eq. (2.7a) with Eqs. (2.8) and (2.11) and substitute the solution

$$\overline{V}_j^n=\begin{pmatrix}u_0\\ w_0\\ \partial_x u_0\\ \partial_x w_0\end{pmatrix}\exp[i(\omega_{num}n\Delta t+kjh)] \tag{C.1}$$

into Eqs. (2.7a), (2.8) and (2.11) with relations (B.1) and (B.2) to obtain the following dispersion equation

$$Det(M)=0. \tag{C.2}$$

Owing to the complexity of elements of the matrix M, here we omit the detail expressions of the matrix M.

From the dispersion relation (C.2), we can obtain the ratio of the numerical velocity to the phase velocity c_0 as follows

$$R=\frac{c_{num}}{c_0}=\frac{\omega_{num}\Delta t}{\alpha\theta}=\frac{\gamma}{\alpha\theta}, \tag{C.3}$$

where α is the Courant number, $\theta=kh$, in which k is the wave number and $h=\Delta x$, and $\gamma=\omega_{num}\Delta t$ is a nonlinear function of space grid step h, seismic frequency, weight parameter η, and the Courant number, and satisfies the dispersion equation (C.2).

2-D homogeneous case

For the 2-D case, we can obtain the dispersion equation of the SSPC under the case of $\Delta x=\Delta z=h$ through similar steps as in the 1-D case. Speaking in detail, considering the

harmonic solution of Eq. (2.7a), we substitute the solution

$$U_{j,l}^{n}=\begin{pmatrix} U_0 \\ \partial_x U_0 \\ \partial_z U_0 \end{pmatrix} \exp[i(\omega_{num} n\Delta t+(k\cos v)jh)+(k\sin v)lh)] \tag{C.4}$$

into Eqs. (2.7a), (2.8), and (2.11) with relations (A.1) to (A.7) to obtain the 2-D dispersion equation. The dispersion equation for the 2-D case includes an independent variable v which is the angle of the plane-wave propagation with respect to the x-axis. The detail derivation for the 2-D the dispersion equation are omitted here, and we only show the ratio of the numerical velocity to the phase velocity R ($R=c_{num}/c_0$) by solving the 2-D dispersion equation. The dispersion curves of the SSPC are shown in Fig. 3, and we also present the dispersion relation curves of the fourth-order SG method for comparison.

References

[1] K. Aki and P. G. Richards, Quantitative Seismology: Theory and Methods, W.H. Freeman & Co., San Francisco, CA (1980).

[2] R. M. Alford, K. R. Kelly and D. M. Boore, Accuracy of finite-difference modeling of the acoustic wave equation, Geophysics, 39 (1974), 834-842.

[3] S. Chen, D. H. Yang and X. Y. Deng, A weighted Runge-Kutta method with weak numerical dispersion for solving wave equations, Commun. Comput. Phys., 7 (2010), 1027-1048.

[4] P. G. Ciarlet, The finite element method for elliptic problems, Amsterdam: North-Holland (1978).

[5] M. A. Dablain, The application of high-order differencing to the scalar wave equation, Geophysics, 51 (1986), 54-66.

[6] M. Dumbser and M. Käser, An arbitrary high order discontinuous Galerkin method for elastic waves on unstructured meshes II. The three-dimensional isotropic case, Geophys. J. Int., 167 (2006), 316-336.

[7] T. Fei and K. Larner, Elimination of numerical dispersion in finite-difference modeling and migration by flux-corrected transport, Geophysics, 60 (1995), 1830-1842.

[8] B. Fornberg, High-order finite differences and pseudo-spectral method on staggered grids, SIAM J. Numer. Anal., 27 (1990), 904-918.

[9] R. J. Geller and N. Takeuchi, Optimally accurate second-order time-domain finite difference scheme for the elastic equation of motion: One-dimensional case, Geophys. J. Int., 135 (1998), 48-62.

[10] S. Gottlieb, C. W. Shu and E. Tadmor, Strong stability-preserving high-order time discretization methods, SIAM Review, 43 (2001), 89-112.

[11] Z. Guan and J. F. Lu, Numerical Methods, Tsinghua University Press (2006).

[12] E. Hairer, S. P. Nørsett and G. Wanner, Solving Ordinary Differential Equations I: Nonstiff Problems, Springer-Verlag Berlin Heidelberg (1993).

[13] D. Komatitsch, C. Barnes and J. Tromp, Simulation of anisotropic wave propagation based upon a spectral-element method, Geophysics, 65 (2000), 1251-1260.

[14] D. Komatitsch and J. P. Vilotte, The spectral element method: An efficient tool to simulate the seismic response of 2D and 3D geological structures, Bull. Seism. Soc. Am., 88 (1998), 368-392.

[15] Y. Konddoh, Y. Hosaka and K. Ishii, Kernel optimum nearly analytic discretization algorithm applied to parabolic and hyperbolic equations, Computers Math. Appl., 27 (1994), 59-90.
[16] S. K. Lele, Compact finite difference scheme with spectral-like resolution, J. Comput. Phys., 103 (1992), 16-42.
[17] E. Priolo, J. M. Carcione and G. Seriani, Numerical simulation of interface waves by high-order spectral modeling techniques, J. Acoust. Soc. Am., 95 (1994), 681-693.
[18] E. Priolo and G. Seriani, A numerical investigation of Chebyshev spectral element method for acoustic wave propagation, Proceedings of the 13th World Congress on Computation and Applied Mathematics, 2 (1991), 551-556.
[19] R. D. Richtmyer and K. W. Morton, Difference Methods for initial Value Problems, Interscience, New York (1967).
[20] A. Sei and W. Symes, Dispersion analysis of numerical wave propagation and its computational consequences, J. Sci. Comput., 10 (1994), 1-27.
[21] P. Solin, K. Segeth and I. Dolezel, Higher-Order Finite Element Methods, Chapman & Hall/CRC Press (2003).
[22] C. W. Shu, Total-variation-diminishing time discretizations, SIAM J. Sci. Statist. Comput., 9 (1988), 1073-1084.
[23] C. W. Shu and S. Osher, Efficient implementation of essentially non-oscillatory shock capturing schemes, J. Comput. Phys., 77 (1988), 439-471.
[24] N. Takeuchi and R. J. Geller, Optimally accurate second order time-domain finite difference scheme for computing synthetic seismograms in 2-D and 3-D media, Phys. Earth Planet. Int., 119 (2000), 99-131.
[25] M. J. Turner, R. W. Clough, H. C. Martin and L. J. Topp, Stiffness and deflection analysis of complex structures, J. Aeronaut. Sci., 23 (1956), 805-823.
[26] J. Virieux, P-SV wave propagation in heterogeneous media: Velocity-stress finite-difference method, Geophysics, 51 (1986), 889-901.
[27] D. H. Yang, E. Liu and Z. J. Zhang, Evaluation of the u-W finite element method in anisotropic porous media, J. Seism. Expl., 17 (2008), 273-299.
[28] D. H. Yang, E. Liu, Z. J. Zhang and J. W. Teng, Finite-difference modeling in two-dimensional anisotropic media using a flux-corrected transport technique, Geophys. J. Int., 148 (2002), 320-328.
[29] D. H. Yang, J. M. Peng, M. Lu and T. Terlaky, Optimal nearly analytic discrete approximation to the scalar wave equation, Bull. Seism. Soc. Am., 96 (2006), 1114-1130.
[30] D. H. Yang, J. W. Teng, Z. J. Zhang and E. Liu, A nearly-analytic discrete method for acoustic and elastic wave equations in anisotropic media, Bull. Seism. Soc. Am., 93 (2003), 882-890.
[31] D. H. Yang, N. Wang, S. Chen and G. J. Song, An explicit method based on the implicit Runge-Kutta algorithm for solving the wave equations, Bull. Seism. Soc. Am., 99 (2009), 3340-3354.
[32] J. Zahradnik, P. Moczo and T. Hron, Testing four elastic finite-difference schemes for behavior at discontinuities, Bull. Seism. Soc. Am., 83 (1993), 107-129.
[33] Z. J. Zhang, G. J. Wang and J. M. Harris, Multi-component wave-field simulation in viscous extensively dilatancy anisotropic media, Phys. Earth & Planet. Inter., 114 (1999), 25-38.
[34] H. S. Zheng, Z. J. Zhang and E. Liu, Non-linear seismic wave propagation in anisotropic media using the flux-corrected transport technique, Geophys. J. Int., 165 (2006), 943-956.